ACS NANO
Cite This: ACS Nano 2018, 12, 317−326
www.acsnano.org

ARTICLE

Controlled Self-Assembly of Photofunctional Supramolecular Nanotubes

Erez Cohen,[†] Haim Weissman,[†] Iddo Pinkas,[‡] Eyal Shimoni,[‡] Pavel Rehak,[§] Petr Král,*[,§,∥] and Boris Rybtchinski*[,†]

[†]Department of Organic Chemistry and [‡]Department of Chemical Research Support, Weizmann Institute of Science, Rehovot 7610001, Israel

[§]Department of Chemistry and [∥]Departments of Physics and Biopharmaceutical Sciences, University of Illinois at Chicago, Chicago, Illinois 60607, United States

Supporting Information

ABSTRACT: **Designing supramolecular nanotubes (SNTs) with distinct dimensions and properties is highly desirable, yet challenging, since structural control strategies are lacking. Furthermore, relatively complex building blocks are often employed in SNT self-assembly. Here, we demonstrate that symmetric bolaamphiphiles having a hydrophobic core comprised of two perylene diimide moieties connected *via* a bipyridine linker and bearing polyethylene glycol (PEG) side chains can self-assemble into diverse molecular nanotubes. The structure of the nanotubes can be controlled by assembly conditions (solvent composition and temperature) and a PEG chain length. The resulting nanotubes differ both in diameter and cross section geometry, having widths of 3 nm (triangular-like cross-section), 4 nm (rectangular), and 5 nm (hexagonal). Molecular dynamics simulations provide insights into the stability of the tubular superstructures and their initial stages of self-assembly, revealing a key role of oligomerization *via* side-by-side aromatic interactions between bis-aromatic cores. Probing electronic and photonic properties of the nanotubes revealed extended electron delocalization and photoinduced charge separation that proceeds *via* symmetry breaking, a photofunction distinctly different from that of the fibers assembled from the same molecules. A high degree of structural control and insights into SNT self-assembly advance design approaches toward functional organic nanomaterials.**

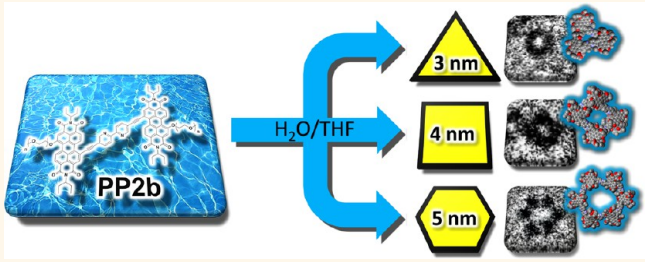

KEYWORDS: *supramolecular materials, self-assembly, nanotubes, supramolecular polymer, photoinduced charge transfer, perylene diimides*

Supramolecular nanotubes (SNTs) represent an important class of noncovalent arrays,[1−7] whose nanoporosity enables capture, storage, transport, and release of different molecular and macromolecular cargos.[6,7] Most tubular assemblies reported so far have diameters ranging from tens of nm to several micrometers, while SNTs having diameters of several nm are rare.[5,8,9] SNTs are typically assembled in aqueous media from monopolar amphiphiles, asymmetric bolaamphiphiles, or macrocycles,[5−7,10,11] while simpler symmetric bolaamphiphiles are rarely employed.[12,13] One of the key challenges in SNT self-assembly is tuning their diameter at the nanoscale[4,5] which is essential to enable accommodation of various molecular cargos. Yet, synthetic schemes to control SNT structures are lacking due to complex assembly mechanisms that are only partially understood.[5,14,15]

Herein, we report a SNT self-assembly from symmetric bolaamphiphiles based on the same hydrophobic core, where precise structural control is enabled by a combination of specific molecular interactions and solvation. This allows precise tuning of tubular structures, including their diameters. Conversion of one type of nanotube into another was also demonstrated. The nanotubes exhibit distinct photophysical behavior (photoinduced charge separation) and show efficient electron delocalization. Molecular dynamics (MD) simulations provide an insight into the stability of the tubular superstructures and their initial stages of self-assembly that involves pairwise side-by-side stacking interactions between several molecular units. This represents a distinctive general mode of molecular interactions leading to tubular assembly based on a bis-aromatic motif.

Received: September 7, 2017
Accepted: December 19, 2017
Published: December 19, 2017

DOI: 10.1021/acsnano.7b06376
ACS Nano 2018, 12, 317−326

RESULTS AND DISCUSSION

We have shown that **PP2b** derivatives with medium-sized PEGs self-assemble into supramolecular polymers in water/THF mixtures.[16] In these systems, aromatic cores stack one on top of the other in register, which is typical for many aromatic amphiphiles.[3] Recently, it has been shown that aromatic amphiphiles can exhibit complex interaction modes, leading to unique assembly structures.[17,18] Our previous work suggested that perylene diimide (PDI) stacking can be controlled in aqueous medium under conditions of kinetic control, leading to nonstacked or stacked systems as a result of organic cosolvent addition/evaporation.[19] We envisioned that in bis-aromatic systems connected by a linker, such as **PP2b** (Figure 1a), interactions between aromatic cores can be attenuated to result in side-by-side stacking (Figure 1b), leading to new supramolecular polymerization modes. For this purpose, we investigated self-assembly of **PEG-PP2b** (PEG13 and PEG44, see Figure 1a) at a wide range of conditions. Bulky PEG44 was expected to partially suppress in-register stacking, while for shorter PEGs, organic cosolvent content was tuned in a broad range in order to control stacking/hydrophobic interactions. Using this methodology, tunable tubular assemblies could be prepared that are based on side-by-side stacking interactions (Figure 1b). Assembly of diverse tubular motifs from symmetric building blocks (see below) contradicts the common SNT design concept, implying that nonsymmetric amphiphiles should be employed for SNT self-assembly.[7]

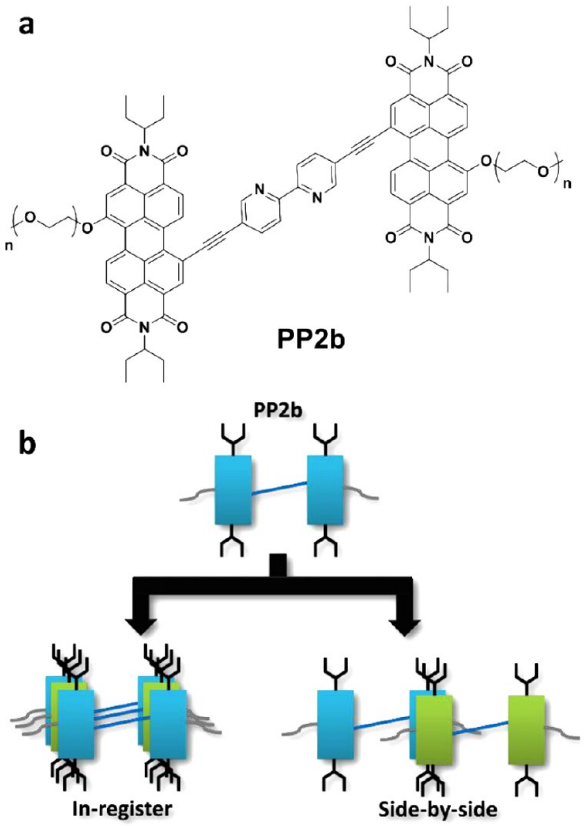

Figure 1. (a) PP2b amphiphile building blocks, PEG lengths: *n* = 13 or *n* = 44. (b) Schematic illustration of PP2b stacking interactions: In-register (left) and side-by-side (right).

First, we investigated self-assembly of **PP2b PEG44** bearing relatively large PEG substituents. Cryogenic transmission electron microscopy (cryo-TEM) imaging of **PP2b PEG44** in neat water revealed the formation of nanotubes with an average width of 4.6 ± 0.3 nm, which were hundreds of nm long at 10^{-3} M concentration (Figure 2a, Figure S1) and mostly tens of nm long at 10^{-4} M (Figure S3). The images are typical of tubular structures: The darker contrast results from higher electron density of the **PP2b** aromatic core stacks (tube walls), while the lighter contrast is due to the tube interior.[17,20−22] Highly hydrated PEGs are normally not observed in cryo-TEM images due to their low contrast.[16,23,24] Occasionally, tubular cross sections are seen in the imaging plane (for tubes that are parallel to the optical axis), revealing the ordered hexagonal structure of the PDI core (Figure 2b,c, Figure S3). Such degree of order and complexity is not typical for symmetric bolamphiphiles.[3] The tubes have a certain propensity to align, typical of rigid rod-like assemblies[24−26] (Figures S1 and S4). In the case of shorter SNTs formed at lower concentrations (10^{-4} M), small bundles of aligned tubes occasionally orient parallel to the optical axis (Figure 2b and Figure S4), while longer tubes (micron-long, formed at higher concentrations, 10^{-3} M) orient mostly perpendicularly to optical axis, as expected based on the thickness of the vitrified water layer (100−150 nm).[27] Similar intertube spacings (~14−15 nm) were observed in the aligned bundles of both longer and shorter tubes (Figure S1 and Figure 2b). High-resolution cryo-TEM cross-section image (dimensions of 5 × 4.6 nm, Figure 2b,c) and molecular modeling (Figure 2d, Figure S2a) suggest that three **PP2b** molecules are stacked on top of another layer of three **PP2b** ones, leading to tubular structure. The darker-contrast spots in the cross-section image (Figure 2c, Figures S3 and S4) correspond to PDI stacks. The cross-section dimensions in the model (Figure 2d) fit well the dimensions observed in cryo-TEM images (Figure 2a−c). The hexagonal tube assemblies convert into molecular fibers within 7 days (Figures S5 and S6), apparently in order to optimize hydrophobic interactions, indicating that the nanotube assembly occurs under kinetic control. The hexagonal SNTs are relatively stable due to high kinetic barriers in aqueous media.[3,28] The addition of THF to the aqueous solution of nanotubes led to vesicles (40% THF, Figure S7a) or large fibrous aggregates (5% THF, Figure S7b), underscoring a critical role of a solvent in aqueous self-assembly.[29] Formation of lower curvature vesicular structures upon addition of an organic cosolvent further confirms that SNTs are formed under kinetic control.[3,28] Importantly, diverse structures can be obtained from a single molecular building block.

In the case of shorter PEG13, **PP2b PEG13** in water:THF = 8:2 (v/v, 10^{-4} M) assembles into molecular fibers (Figure S8). In contrast, **PP2b PEG13** in water:THF = 6:4 (v/v, 10^{-4} M) forms nanotubes with rectangular cross sections that have an average width of 3.5 ± 0.4 nm and are hundreds of nm in length (Figure 3a,b and Figure S9). The dimensions of the rectangular cross-section (3.7 × 3.2 nm) correspond well to those in the model (3.9 × 3.3 nm, Figure 3c). Cryo-TEM imaging and molecular modeling (Figure 3c, Figure S2b) suggest that two parallel **PP2b** molecules are stacked on top of another perpendicularly oriented pair of **PP2b** molecules, eventually forming a nanotube with a rectangular cross-section. The width of the inner cavity in the model is 0.8 nm (the dimensions of the inner cavity observed in high-resolution cryo-TEM images are difficult to estimate due to contrast limitations; it appears to be <1.5 nm). Interestingly, a transformation of the rectangular tubes (4 nm in diameter,

DOI: 10.1021/acsnano.7b06376
ACS Nano 2018, 12, 317−326

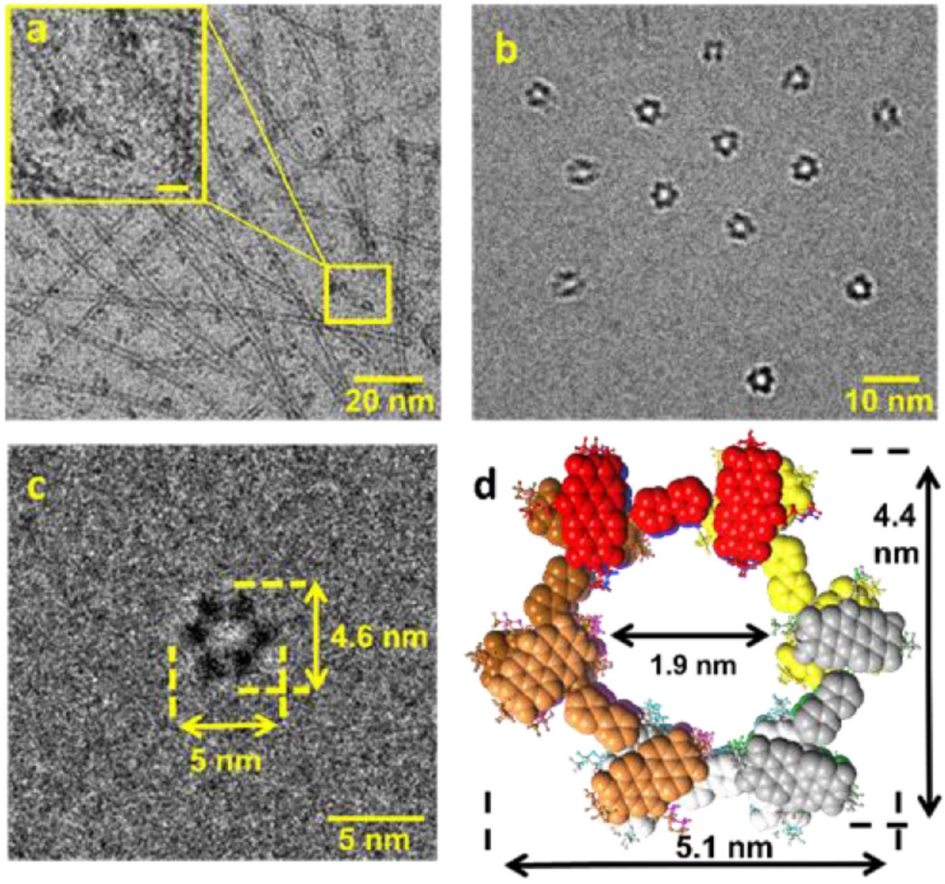

Figure 2. Cryo-TEM images (a–c) and proposed molecular model (d) of self-assembled PP2b PEG44 nanotubes in neat water. (a) 10^{-3} M, aging 75 min, side view, showing tubes with outer diameter of 4.6 ± 0.3 nm (cross section 5.0 ± 0.1 nm). Inset: magnified image showing connection of a cross-section and a tube wall. Scale bar is 5 nm. (b) 10^{-4} M, aging 5 h, hexagonal cross section. For zoomed out and enlarged images see Figure S4. (c) High-resolution hexagonal cross section. The tube outer dimensions are 5.0 × 4.6 nm. Molecular model: (d) Cross-section, top view. The geometry was optimized using molecular mechanics (augmented MM2 and MM3 parameters). For computational simplification, PEG chains were modeled as $-O(CH_2-CH_2)OCH_3$ groups. The aromatic core in the model is given in a space-filling representation.

Figure S10) into larger (4.8 ± 0.4 nm diameter) and more rigid ones (almost no bending observed) was achieved by heating the assembly at 55 °C for 30 min (Figure 4 and Figure S11). The resultant tubes are stable and do not change upon further heating. These nanotubes were also observed by SEM imaging, revealing diameters of 6.5 ± 0.8 nm (Figure S12), where the larger diameter is consistent with the presence of PEG chains (wrapping the SNTs) that become visible in SEM images. The nanotubes may have hexagonal cross-section (not seen in cryo-TEM images), as they are rigid and exhibit diameters close to the ones of the rigid hexagonal tubes based on **PP2b PEG44**.

To further control the SNT structures, mixing PEG13 and PEG44 **PP2b** was employed. Our rational for the mixing relies on the fact that when the hydrophilic parts of a **PP2b** amphiphile molecule become larger, the molecule gains a wedge-like shape, and one can obtain increasing curvature of the self-assembled structures.[30] Thus, we added small amounts of **PP2b PEG44** to **PP2b PEG13**. The samples were prepared using co-evaporation and redispersion, wherein **PP2b PEG44** and **PP2b PEG13** in disaggregating solvent ($CHCl_3$) were premixed, dried in vacuum, and then assembled as follows. The mixture was first dissolved in THF, followed by fast addition of water and vigorous mixing. A mixture of 5% **PP2b PEG44**/ 95% **PP2b PEG13** (40% THF, 10^{-4} M) was found to form nanotubes with an average width of 3.2 ± 0.2 nm and lengths of hundreds of nm (Figure 3d, Figure S13).

The observed cross-section (Figure 3d) and molecular modeling (Figure 3f, Figure S2c) suggest a structure in which three **PP2b** molecules are stacked in a helical arrangement with a triangle-like geometry and a twisting angle of 120° relative to each other. This structure results in a helical tube (Figure 3f) with an outer diameter of 3.1 nm and an inner one of roughly 0.3 nm, in agreement with the cryo-TEM imaging. The observed fine structure of the nanotubes (Figure S13d) appears to be compatible with helical packing. We note that resolution of cryo-TEM images precluded further unequivocal confirmation of helicity and precise determination of SNTs' inner diameters. The absence of self-sorting in this system (formation of two distinct aggregate types) is probably due to strong driving forces that result in efficient irreversible interactions between all moieties.[31]

Unlike the rectangular ones, these nanotubes are stable at 55 °C (Figures S15–S17, see summary of SNTs properties in Table 1). Our attempts to further control the structure by altering the **PP2b PEG44**/**PP2b PEG13** ratio resulted in diverse assemblies. For instance, increasing the **PP2b PEG44** content to 10% leads to molecular fibers (1% THF, Figure S18a) or a dense 3D network of fibers (40% THF, Figure S18b). Likewise, the ratio of 95% **PP2b PEG44**/ 5% **PP2b**

DOI: 10.1021/acsnano.7b06376
ACS Nano 2018, 12, 317–326

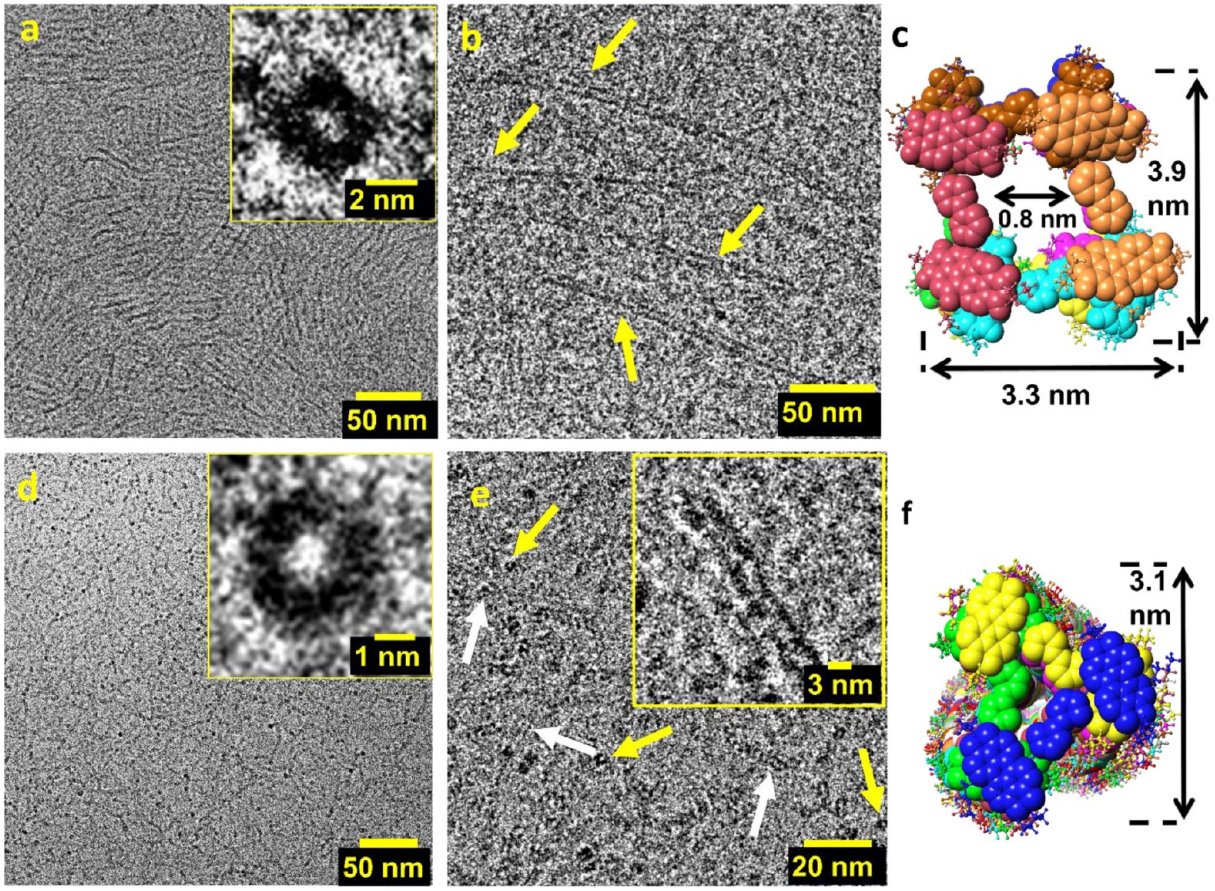

Figure 3. Cryo-TEM images (a, b, d, e) and proposed molecular models (c, f) of self-assembled PP2b PEG13 and 5% PP2b PEG44/ 95% PP2b PEG13 nanotubes in water:THF = 6:4 (v/v, 10^{-4} M). (a) Lower magnification. Inset: Rectangular cross-section, outer dimensions are 3.7 × 3.2 nm. (b) Aging 3 h, tubes with outer diameter of 3.5 ± 0.4 nm (cross section 3.5 ± 0.1 nm). Yellow arrows: tubes (darker-contrast). (c) Molecular model cross-section. (d) Lower magnification. Inset: "triangular" (helical) cross-section. The tube outer diameter is 3.3 nm. (e) Aging 3 h, showing tubes with outer diameter of 3.2 ± 0.2 nm (cross section 3.1 ± 0.1 nm). Yellow arrows: cross section; white arrows: tubes, oriented permendicularly to the optical axis. Inset: Magnified image of a nanotube. (f) Molecular model cross-section. The geometry was optimized using molecular mechanics (augmented MM2 and MM3 parameters). For computational simplification, PEG chains were modeled as $-O(CH_2-CH_2)OCH_3$ groups. The aromatic core in the model is given in a space-filling representation, corresponding to the darker contrast in the images.

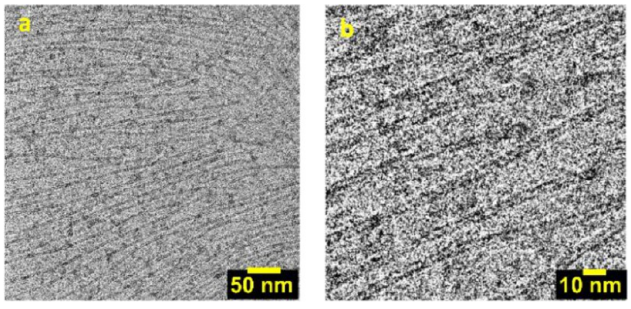

Figure 4. (a, b) Cryo-TEM image of self-assembled PP2b PEG13 nanotubes in water:THF = 6:4 (v/v, 10^{-4} M) aging 8.5 h after heating to 55 °C for 30 min. Average width 4.8 ± 0.4 nm.

PEG13 resulted in molecular fibers (1% THF, Figure S19a) or vesicles (40% THF, Figure S19b).

UV−vis absorption spectroscopy (Figure S20) indicated that all three tubular structures show the inversion of relative intensities of 0−0 and 0−1 vibronic bands, which is typical for face-to-face stacking of PDI cores,[32] consistent with the proposed SNT structures. Electron delocalization properties of the long 5 nm-wide nanotubes assembled from **PP2b PEG13** (40% THF, 10^{-4} M, heated to 55 °C for 30 min, Figure S11) were examined by electron paramagnetic resonance (EPR) spectroscopy. Reducing **PP2b PEG13** with subequivalent amount of $Na_2S_2O_4$ resulted in paramagnetic PDI radical anions generated within the assemblies as detected by both EPR and UV−vis absorption spectroscopy (Figure 5a, Figure S21a).[33,34] Comparison of the EPR peak widths of the aggregated and disaggregated solutions revealed electron delocalization over four molecules.[35,36] Upon exposing the partially reduced samples to air, the radical anions were oxidized back to the neutral state and the typical absorption of the aggregated solution appeared, indicating a reversible reduction/oxidation process (Figure S21a).

To gain an insight into the excited-state dynamics, we performed femtosecond (fs) and nanosecond (ns) transient absorption (TA) studies on the longest and most stable SNTs. These are 5 nm wide **PP2b PEG13** nanotubes (40% THF, 10^{-4} M) that form following heating to 55 °C for 30 min (Figure 4). The fsTA spectra (Figure 5b, excitation at 590 nm) exhibit negative ground-state bleach centered at 540 nm and a positive excited-state feature in the NIR region. The appearance of a peak at ∼760 nm and the fact that a broad peak at 680 nm (PDI excited-state absorption) quickly decays

DOI: 10.1021/acsnano.7b06376
ACS Nano 2018, 12, 317−326

Table 1. Summary of SNTs Properties

tube composition	solvent	cross section geometry	diameter (nm)	stability
PP2b PEG13	6:4 water/THF (v/v)	rectangular	3.5 ± 0.4	stable at rt
PP2b PEG13 (heated to 55 °C for 30 min)	6:4 water/THF (v/v)	probably hexagonal	4.8 ± 0.4	stable
5% **PP2b PEG44**/ 95% **PP2b PEG13**	6:4 water/THF (v/v)	triangle-like	3.2 ± 0.2	stable
PP2b PEG44	water	hexagonal	4.6 ± 0.3	kinetically stable, transform gradually to molecular fibers

("shifts to the red", Figure 5b), while the 760 nm feature has a substantially longer lifetime (3−4 ns, Figure S21c,d), is typical of PDI radical anion formation, occurring *via* symmetry-breaking charge transfer.[37,38] The SNT fsTA kinetics does not show a power dependence attributable to exciton hopping (Figure S21b),[39] in contrast to segmented fibers based on **PP2b PEG17**, reported earlier.[16] The charge transfer in the nanotubes occurs with ∼24% yield, according to kinetic analysis at 760 nm (Figure 5c, Tables S1 and S2). The observed photoinduced symmetry-breaking charge separation[40] in electron-deficient PDI-based systems is rare,[37,38] since, normally, this process is not thermodynamically favorable. The fast time scale of the symmetry breaking in the nanotubes (∼0.9 ps) may be aided by highly efficient charge delocalization over four molecules. In contrast, femtosecond TA studies of molecular fibers based on **PP2b PEG13** (20% THF, 10^{-4} M, Figure S22) reveal a low yield of photoinduced charge separation (∼5% according to kinetic analysis at 750 nm, Table S3) and shorter lifetimes. This occurs despite the fact that the fibers exhibit efficient electron delocalization over eight PDI molecules (Figure S23), according to our EPR study. One possible explanation for the observed difference in photoinduced charge transfer (PCT) could be attributed to the structural variations between the assemblies, with adjacent stacked PDIs in the tubes experiencing slightly different environments, unlike in the fibers.

Further studies aimed at elucidating the PCT behavior in the nanotubes involved the addition of an electron donor (triethylamine, TEA, 4%, v/v) to a solution of **PP2b PEG13** nanotubes (40% THF, 10^{-4} M) after heating to 55 °C for 30 min (Figure 4). The fsTA spectra (Figure S24, excitation at 590 nm) exhibit different features compared with the case without an external electron donor. Thus, no red-shift of PDI peaks typical of PDI symmetry breaking was observed. As expected, fast PCT occurs as indicated by the appearance of 760 nm band. PCT state has much shorter lifetime than that in the absence of TEA (Table S4). This underscores a difference with regard to a symmetry breaking state. Longer lifetime of the latter may be due to charge delocalization within PDI stacks. Different reorganization energies (PDI and solvent) may also contribute to the observed difference. We note that the reported electron-deficient PDI systems showing symmetry-breaking charge transfer are small well-defined molecular arrays.[37,38] Extended 1D nanostructures such as SNTs that are built from a single type of robust chromophores and exhibit longer PCT life times may enable new approaches to optoelectronic wires, expanding the range of SNT functions.

In order to gain mechanistic molecular-scale insight into the self-assembly of different **PP2b** molecules and the stability of molecular superstructures formed, we used all-atom molecular dynamics (MD) simulations in explicit solvent to model: (i) the process of **PP2b** molecular self-assembly and (ii) the spatial organization of molecular/solvent components in the self-assembled superstructures (see Supporting Information). For **PP2b PEG44** (Figure 6a,b, neat water), the simulations show the outcome for 12 monomers self-assembling for 150 ns in a water box of 5,400 nm^3 (see computational details in Methods and Supporting Information). The simulations revealed that within 10 ns **PP2b PEG44** formed a large cluster, resembling a micelle,[41,42] where the hydrophobic **PP2b** moieties closely interacted, while the long PEG chains surrounded the core of the cluster. Within 22 ns, a first **PP2b** dimer featuring two stacked PDIs (side-by-side arrange-

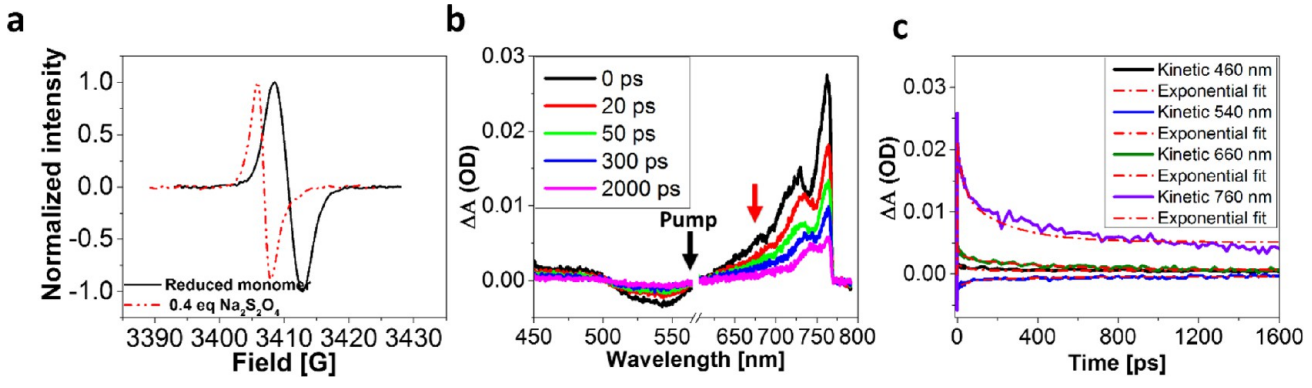

Figure 5. EPR and TA (pumped at 590 nm) of self-assembled PP2b PEG13 nanotubes in water:THF = 6:4 (v/v, 10^{-4} M), heated to 55 °C for 30 min. (a) EPR spectra of reduced: monomer with 4% v/v Et_3N (black), assembly with 0.4 equiv $Na_2S_2O_4$ (red). The electron delocalization length is four molecules. (b) Femtosecond TA spectra evolution over time, 1.5 mW. Red arrow indicates the PDI excited-state peak decay that occurs before the PDI radical anion peak (at 760 nm) decay. (c) Femtosecond TA decay kinetics probed at four wavelengths and their multiexponential fit, 1.5 mW. For details on decay coefficients see Table S1.

DOI: 10.1021/acsnano.7b06376
ACS Nano 2018, 12, 317−326

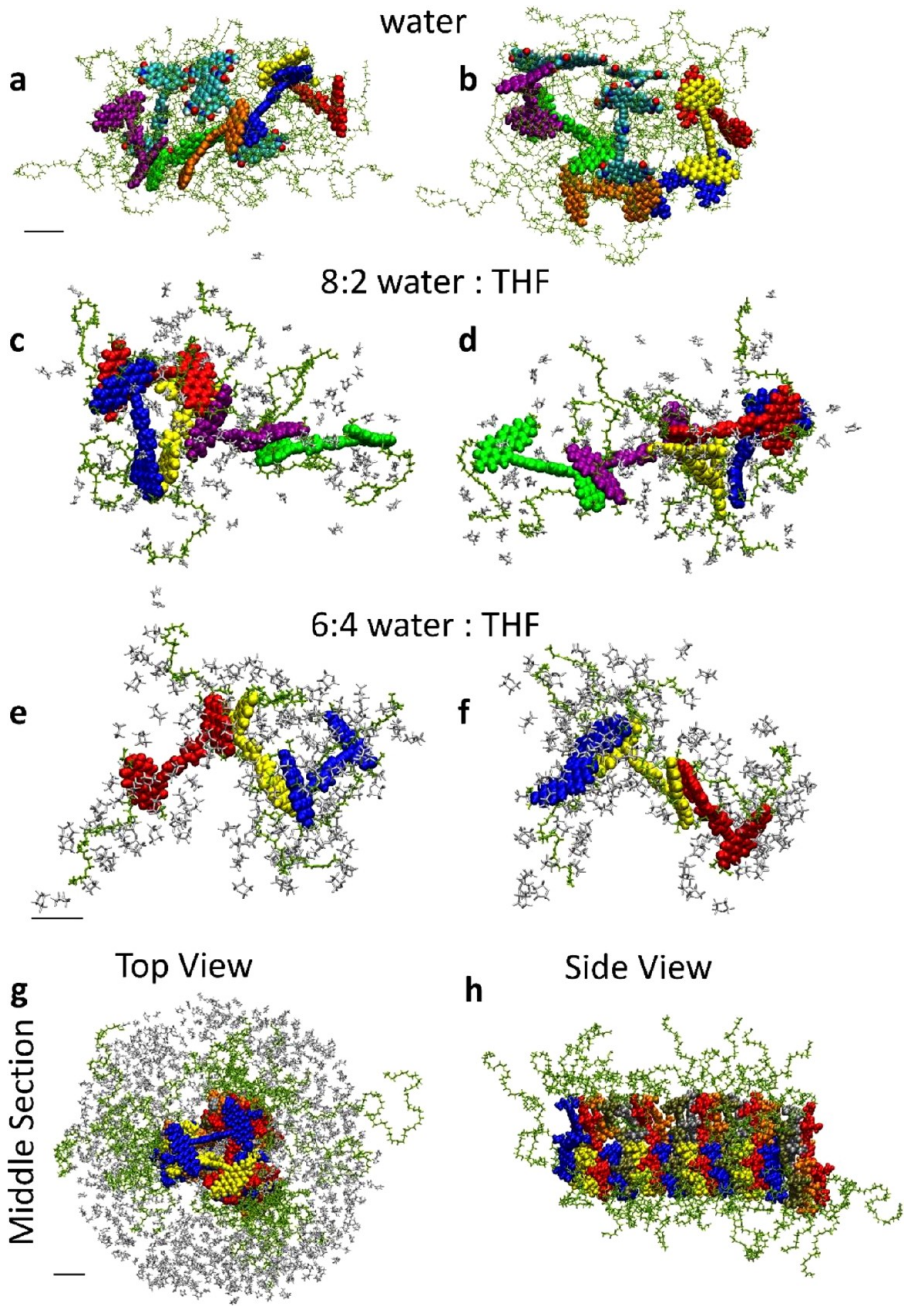

Figure 6. MD simulations of the self-assembly of PEG-ylated PP2b monomers. PP2b molecules are vividly colored, PEG chains are shown in a finer representation, and gray structures represent THF molecules. Scale bars are 1 nm. (a, b) Two views of the main cluster core formed from PP2b PEG44 monomers in pure water at 150 ns. (c, d) Two views of the main cluster core formed from PP2b PEG13 monomers in water:THF solvent at 266 ns. (e, f) Two views of the main cluster core formed from PP2b PEG13 monomers in water:THF = 6:4 (v/v) at 674 ns. (g, h) MD simulations of a fragment (middle section) of a SNT pre-assembled from PEG-ylated PP2b monomers. Top and side views of helical superstructures of 29 PP2b PEG13 and 1 PP2b PEG44 in water:THF = 6:4 (v/v) at 20 ns. For clarity, in a side view, the solvent molecules are not shown.

ment) formed within the core, which was followed by the formation of a trimeric chain at 25 ns. Around 70 ns, another monomer joined the trimer to form a jiggling linear tetramer. At 88 and 115 ns, additional dimers formed outside and within the cluster core, respectively. The rigid and flat bipyridine (bipy) linker was found to promote initial stacking interactions (see Supporting Information for details), eventually leading to side-by-side stacking of PDI moieties resulting in stable oligomers. The rigid nature of the linker most probably restricts a range of possible geometries, promoting oligomer cyclization that eventually leads to nanotubes.

In the case of **PP2b PEG13** (Figure 6c,d), the simulations show the results for 6 **PP2b PEG13** monomers after self-assembling for 266 ns in a water:THF = 8:2 (v/v) solvent in a box of 2200 nm^3. These monomers with shorter PEG chains quickly formed pairs, before forming larger clusters, surrounded by THF molecules (better solvent for hydrophobic cores). The first dimer formed at 12 ns, a second dimer formed at 27 ns, and a trimer formed from the second dimer at 66 ns.

DOI: 10.1021/acsnano.7b06376
ACS Nano 2018, 12, 317−326

Later on, at 185 ns, this trimer formed a closed triangle. The structures formed were also relatively rigid. Simulations of **PP2b PEG13** (Figure 6e,f) show the outcome for 5 **PP2b PEG13** monomers which self-assembled at 674 ns in the water:THF = 6:4 (v/v) solvent in a box of 560 nm^3. Here, the first dimer appeared only at 40 ns, a trimer at 150 ns (shown), and a second dimer only at 544 ns. Figure 6c,f also reveals a close distribution of THF molecules around the PDI cores. These results indicate that with the increasing concentration of a stabilizing THF solvent, the PDI dimerization *via* stacking is a much slower process in comparison with water:THF = 8:2 system, indicating importance of specific solvation. Simulations of the fully assembled tubes (Figure 6g,h, Figures S25 and S26) support our experimental results. They show that the 3 nm (triangular-like, Figure 6g,h) and 5 nm (hexagonal) SNTs are more stable compared with a more flexible 4 nm (rectangular) tube. The latter is in accordance with the experimentally observed transformation of rectangular to the hexagonal tubes upon heating. The high stability of the hexagonal SNTs may be due to highly ordered (crystalline-like) structures, while the triangular-like SNTs (Figure 6g,h) may be stabilized by helical arrangement.

Overall, our simulations confirm that the formation of **PP2b** PEG assemblies is driven by side-by-side $\pi-\pi$ stacking/hydrophobic interactions between the PDI groups leading to supramolecular oligomerization, which is a common process in all systems. Once the interaction has been established, it cannot be easily reversed. Importantly, *pairwise noncovalent interactions leading to side-by-side stacking appear to be a general initial step in oligomerization of bis-aromatic systems*, reminiscent of supramolecular polymerization of molecules bearing bifunctional noncovalent binding motif.[43] The insight into aromatic oligomerization in aqueous media and its relevance to tubular self-assembly has not been observed so far. Complete ring closure was not observed at the explored time scales as such nucleation events are slow and in general are difficult to observe in MD simulations.[44] Further MD studies aimed at elucidating the mechanism of tubular assembly are necessary in order to understand the entire assembly progression.

CONCLUSIONS

In conclusion, we have shown that symmetric bolaamphiphiles are capable of assembling into a variety of nanometer-scale nanotubes. Our experimental and theoretical studies reveal that an interplay of molecular structure and solvation specifics have a profound effect on self-assembly. This enabled tuning of molecular nanotube structures based on identical hydrophobic cores. Additionally, photoinduced symmetry-breaking charge transfer was observed in SNTs, demonstrating that SNTs enable photoactive wire function. Simplification of molecular design, control *via* self-assembly conditions, and photofunction provide tools to create complex functional supramolecular systems.

METHODS

Solvents and reagents were purchased from commercial sources and used as received, unless stated otherwise. For all aqueous mixtures, double-distilled water was used (Barnstead NANOpure Diamond water system). All procedures with air-sensitive compounds were performed under inert gas atmosphere (dried N_2) using a glovebox (MBRAUN, Labmaster). Organic solvents used for these procedures were degassed with argon and stored over molecular sieves (4 Å) in the glovebox. Synthesis of **PP2b** derivatives was reported previously.[45]

UV−vis Absorption Measurements. Measurements were carried out on a Cary-5000 spectrometer (Varian).

Cryo-TEM. Cryo-TEM was carried out using a Tecnai T12 transmission electron microscope operating at 120 kV with a Gatan OneView 4k × 4k digital camera Model 1095, or Tecnai F20 transmission electron microscope operating at 200 kV with a Gatan US4000 digital camera. Samples were transferred using a transfer station to a Gatan 626 cooling holder and introduced into the microscope. Sample preparation: 6 μL of sample solution was applied to a 200 mesh copper grid coated with holey carbon (Pacific Grid-Tech) and was blotted at 25 °C (95% humidity), and then the grid was immediately plunged into liquid ethane using a Leica EM-GP Auto plunger. Image analysis was done using iTEM software (v 5.2 build 3554, Olympus).

Freeze-Dry cryo-SEM. A drop of 3 μL of **PP2b PEG13** nanotubes in 60:40 water/THF (v/v), 10^{-4} M aging 3 h after heating to 55 °C for 30 min was deposited on a nitrocellulose-coated 200 mesh copper EM grid, blotted with a filter paper, and plunged into liquid ethane using a custom-made plunger (Technion, Israel Institute of Technology, Israel).

The grids were then transferred to a BAF 60 freeze fracture device (Leica Microsystems, Vienna, Austria) using a VCT 100 Cryo transfer shuttle (Leica Microsystems) and sublimed at a temperature of −80 °C and pressure of 1×10^{-6} mbar for about 1 h. The sample was transferred to a GeminiSEM 500 scanning electron microscope (Carl Zeiss AG, Oberkochen, Germany) equipped with a Cryo stage (Leica Microsystems). Samples were observed without or with coating with a layer of 2 nm Pt/C (coating was conducted at the BAF 60) at acceleration voltages ranging between 0.7 and 1.5 kV using an InLens secondary electrons detector.

Molecular Modeling Computations. Molecular mechanics (MM) geometry optimizations were carried using augmented MM3 parameters followed by augmented MM2 parameters with Fujitsu Scigress v 2.2. For computational simplification, PEG chains were modeled as $-O(CH_2-CH_2)OCH_3$ groups.

EPR. Electron paramagnetic resonance spectra were measured with a Bruker E-580 spectrometer equipped with an EN801 resonator at 298 K. Aggregated solutions of deoxygenated THF/water were reacted with 0.1 and 0.02 equiv sodium dithionite, while disaggregated THF solution was loaded with 4% v/v triethylamine (TEA) and excited by high power LED (150W, 2 min) according to a literature procedure.[46] All samples were measured in 0.8 mm capillary tube sealed before the EPR measurements in nitrogen-filled glovebox.

Transient Absorption. The system is based on a modelocked Ti:sapphire oscillator (Spectra Physics Mai Tai SP). The oscillator produces a train of <120 fs pulses (bandwidth ∼12 nm fwhm), with a peak wavelength at 800 nm, typically of 900 mW, corresponding to ∼10 nJ per pulse. The weak oscillator pulses are amplified by a chirped pulse regenerative amplifier (CPA) (Spectra Physics Spitfire ACE). The pulse is first stretched to several picoseconds and then is regeneratively amplified in a Ti:sapphire cavity, pumped by a pulsed Nd:YLF laser (Spectra Physics Empower 45) operating at 1 kHz. After the pulse has been amplified and recompressed, its energy is about 5 mJ in a train of 1000 Hz pulses. An independent pump pulse is obtained by pumping an optical parametric amplifier (Light Conversion, TOPAS-Prime, and NIRUVIS harmonic generator) that produces 120 fs pulses continuously tunable from 300 nm to 3 μm. The output power of the OPA varies between a few micro Joules to tens of micro Joules (depending on the chosen wavelength) at 1000 Hz. The probe beam is mechanically chopped at half the amplifier repetition rate. The chopper (C-995 TTI) is synchronized to the Spitfire amplifier. Normally a few thousand pulse pairs (pump on/pump off) are averaged to produce a TA spectrum with a noise level below 0.3 mOD. A small portion of the remaining amplified pulse is used to generate a white light continuum as a probe pulse. To this end, the Ti:sapphire beam is focused onto a 3 mm-thick CaF_2 window by a 5 cm focal length lens, and the numerical aperture of the beam is controlled by an iris placed in front of the lens, which helps to obtain a stable and smooth white light continuum. In order to avoid thermal damage on the CaF_2 window and noise in the continuum white light,

DOI: 10.1021/acsnano.7b06376
ACS Nano 2018, 12, 317−326

it is moved in a circular motion so that each consecutive laser pulse hits a fresh spot. The system returns to the same location every few tens of seconds. The resulting beam is passed through a Raman notch filter to remove the remains of the fundamental beam from the probe white light continuum. The pump and probe pulses are crossed in the sample at a small angle, while maintaining a magic angle between the pump and probe polarizations. The remains of the pump pulse are removed by an iris, and the probe light is imaged onto an optical fiber that brings it into an imaging interface, which focuses the light onto the entrance slit of a Jobin Yivon Triax 180 spectrograph. The light is normally dispersed by a 300 gr/mm grating onto a fast CCD camera (Andor Newton DU-920P-BEX2-DD, operating at 1000 spectra per second using "crop mode"). The TA setup is controlled by National Instruments LabView software. A variable neutral-density filter was employed to adjust the pump power. The pump power intensities were measured using Ophir photodiode sensor power meter in proximity to the sample. The excitation densities were estimated for a laser spot of 300 μm diameter on the sample. This diameter was measured by placing beam profiler (Ophir Beamstar FX33) at the sample position and determining the 4-σ (95% of the power) parameter. In the reported experiments, the pump was turned to 590 nm, and the optical densities of the samples, in 1 and 2 mm optical path length cuvettes, were kept between 0.2 and 0.4 at the excitation wavelength. Spectral corrections and analysis were performed using Surface Xplorer Pro (Ultrafast Systems) and Origin 9.1 (OriginLab) software.

The ns−μs data were collected using the same laser as a pump source (from oscillator to OPA), and the detection was done in an EOS subnanosecond TA spectrometer (Ultafast Systems, USA). The spectrometer has a 100 ps instrument response and allows for the measurement of TA between 400 and 900 nm. Data analysis was done as mentioned before.

Molecular Dynamics. MD simulations were performed with NAMD[3] package, using the CHARMM force field.[47−51] Internal molecular and dispersion parameters were taken from the CHARMM 36 general force field.[52] Due to difficulties of *ab initio* frequency calculations of alkyne and extended aromatic groups in the **PP2b** core, missing parameters were approximated using the parachem software.[51] *Ab initio* calculations using Gaussian 09[53] package were performed on the linker group between the two extended aromatic groups, the extended aromatic groups themselves, and the terminal noncyclical aromatic ring, using MP2/6-31g(d)//MP2/6-31g(d) level of theory to determine partial charges of **PP2b** core using the ChelpG algorithm.[54] CHARMM TIP3P water model was employed for explicit water simulations.

Two types of simulations were performed: (i) self-assembly and (ii) superstructure simulations. In the self-assembly system, each of the **PP2b** molecules were placed and rotated randomly in their respective environment. PEGylated chains with 44 oxygen atoms were simulated in pure water, whereas PEGylated chains with 13 oxygen atoms were placed in water/THF mixtures. There were two different mixtures of water and THF: (i) 60% water: 40% THF (v:v) and (ii) 80% water: 20% THF (v:v). Experimental density[55] of pure THF was used to determine the number of THF molecules per system. The volume of each system was determined by placing the **PP2b** molecules and then adding 3 nm to the maximum and minimum coordinate values of the **PP2b** molecules.

A total of three self-assembly systems were constructed (i) with pure water and 12 **PP2b** molecules with PEGylated chains, having 44 oxygen atoms, (ii) in 60% water and 40% THF with 8 **PP2b** with PEGylated chains, having 13 oxygen atoms, and (iii) in 80% water and 20% THF with 6 **PP2b** molecules, with PEGylated chains, having 13 oxygen atoms. A total of three superstructure simulations were constructed (i) hexagonal structure (Figure 2 of the main text) with PEGylated chains 44 oxygen atoms long in pure water, (ii) square structure (Figure 3a,c of the main text) in 60% water: 40% THF (v:v), (iii) square structure (actually giving rise to molecular fibers, Figure S8) in 80% water: 20% THF (v:v). Because those superstructures had the PEGylated chains of $-O(CH_2-CH_2)OCH_3$ groups, additional PEGylated links were added until desired length was achieved.

Water and THF were initially placed immiscibly ,and during minimization and pre-equilibration they were allowed to diffuse without any constrains until the solvent was homogeneous. During minimization (50,000 steps) and pre-equilibration (at least 3 ns), only atoms in the **PP2b** core were subjected to constraints, whereas the solvent molecules and PEGylated chains were allowed to move without any constraints. During the production runs, the self-assembly molecules had no constraints; in the superstructure simulations, only the linking bipyridine carbons and the nitrogen atoms on the bipyridine group, on one molecule per superstructure, were constrained, with 20% of value of the constraints employed during minimization.

Simulations were done with NPT ensemble at a temperature of 310 K and a pressure of 1 atm and periodic boundary conditions. Langevin dynamics were used to maintain pressure and temperature, with a damping constant of 1 ps^{-1}, temperature bath was 310 K, hydrogen atoms were excluded from the thermal bath, piston period was 100 fs, piston decay was 50 fs. Excluding minimization, particle mesh Ewald[56] was used with a grid spacing of 1.0. Velocity Verlet integrator was used to solve equations of motion, with a time step of 2 fs. The SHAKE algorithm was used for the hydrogen atoms. Nonbonded interaction used the switching algorithm, with the switch-on distance at 10 Å and the switch-off at 12 Å. Nonbonded pair lists were used for atoms within 13.5 Å of each other, with the list updated every 20 steps. 1−4 nonbonded interactions were not scaled. Data and snapshots were recorded every 10 ps or every 5000 steps. The pure water simulation system lasted 200 ns, due its computational expense, whereas all other systems were 300 ns or longer. In order to improve efficiency of the simulations, the size of the 60% water self-assembly system was first decreased by excluding only solvent molecules, but the number of **PP2b** molecules was kept constant. Subsequently the size was further decreased from eight molecules to only five **PP2b** molecules. When constructing the superstructure for the aqueous system, the original length of the PEGylated chains was lengthened to 44 oxygen atoms, in an extended conformation. Then the superstructure was allowed to minimize and equilibrate in vacuum, so that the PEGylated chains would fold onto the superstructure, thus requiring a smaller volume for the simulation.

ASSOCIATED CONTENT

Supporting Information

The Supporting Information is available free of charge on the ACS Publications website at DOI: 10.1021/acsnano.7b06376.

Experimental details, electron microscopy images, UV−vis absorption spectra, EPR, femtosecond and nanosecond TA spectra, kinetic analysis and MD (PDF)

AUTHOR INFORMATION

Corresponding Authors

*E-mail: boris.rybtchinski@weizmann.ac.il.

*E-mail: pkral@uic.edu.

ORCID

Petr Král: 0000-0003-2992-9027

Boris Rybtchinski: 0000-0002-2071-8429

Notes

The authors declare no competing financial interest.

ACKNOWLEDGMENTS

This work was supported by the Israel Science Foundation and the Helen and Martin Kimmel Center for Molecular Design. The SEM and TEM studies were conducted at the Irving and Cherna Moskowitz Center for Nano and BioNano Imaging (Weizmann Institute). P.K. acknowledges the NSF Division of Materials Research grant 1506886. We thank Dr. R. Carmieli for his help with EPR studies.

DOI: 10.1021/acsnano.7b06376
ACS Nano 2018, 12, 317−326

REFERENCES

(1) Hill, J. P.; Jin, W.; Kosaka, A.; Fukushima, T.; Ichihara, H.; Shimomura, T.; Ito, K.; Hashizume, T.; Ishii, N.; Aida, T. Self-Assembled Hexa-Peri-Hexabenzocoronene Graphitic Nanotube. *Science* **2004**, *304*, 1481−1483.

(2) Jin, W.; Yamamoto, Y.; Fukushima, T.; Ishii, N.; Kim, J.; Kato, K.; Takata, M.; Aida, T. Systematic Studies on Structural Parameters for Nanotubular Assembly of Hexa-Peri-Hexabenzocoronenes. *J. Am. Chem. Soc.* **2008**, *130*, 9434−9440.

(3) Krieg, E.; Bastings, M. M. C.; Besenius, P.; Rybtchinski, B. Supramolecular Polymers in Aqueous Media. *Chem. Rev.* **2016**, *116*, 2414−2477.

(4) Beingessner, R. L.; Fan, Y.; Fenniri, H. Molecular and Supramolecular Chemistry of Rosette Nanotubes. *RSC Adv.* **2016**, *6*, 75820−75838.

(5) Shimizu, T.; Masuda, M.; Minamikawa, H. Supramolecular Nanotube Architectures Based on Amphiphilic Molecules. *Chem. Rev.* **2005**, *105*, 1401−1444.

(6) Bong, D. T.; Clark, T. D.; Granja, J. R.; Ghadiri, M. R. Self-Assembling Organic Nanotubes. *Angew. Chem., Int. Ed.* **2001**, *40*, 988−1011.

(7) Kameta, N.; Minamikawa, H.; Masuda, M. Supramolecular Organic Nanotubes: How to Utilize the Inner Nanospace and the Outer Space. *Soft Matter* **2011**, *7*, 4539−4561.

(8) Barclay, T. G.; Constantopoulos, K.; Matisons, J. Nanotubes Self-Assembled from Amphiphilic Molecules *via* Helical Intermediates. *Chem. Rev.* **2014**, *114*, 10217−10291.

(9) Eisele, D. M.; Arias, D. H.; Fu, X.; Bloemsma, E. A.; Steiner, C. P.; Jensen, R. A.; Rebentrost, P.; Eisele, H.; Tokmakoff, A.; Lloyd, S.; Nelson, K. A.; Nicastro, D.; Knoester, J.; Bawendi, M. G. Robust Excitons Inhabit Soft Supramolecular Nanotubes. *Proc. Natl. Acad. Sci. U. S. A.* **2014**, *111*, E3367−E3375.

(10) Kim, H.-J.; Kang, S.-K.; Lee, Y.-K.; Seok, C.; Lee, J.-K.; Zin, W.-C.; Lee, M. Self-Dissociating Tubules from Helical Stacking of Noncovalent Macrocycles. *Angew. Chem., Int. Ed.* **2010**, *49*, 8471−8475.

(11) Liu, Z.; Liu, G.; Wu, Y.; Cao, D.; Sun, J.; Schneebeli, S. T.; Nassar, M. S.; Mirkin, C. A.; Stoddart, J. F. Assembly of Supramolecular Nanotubes from Molecular Triangles and 1,2-Dihalohydrocarbons. *J. Am. Chem. Soc.* **2014**, *136*, 16651−16660.

(12) Ponnuswamy, N.; Pantoş, G. D.; Smulders, M. M. J.; Sanders, J. K. M. Thermodynamics of Supramolecular Naphthalenediimide Nanotube Formation: The Influence of Solvents, Side Chains, and Guest Templates. *J. Am. Chem. Soc.* **2012**, *134*, 566−573.

(13) Tian, Z.; Li, H.; Wang, M.; Zhang, A.; Feng, Z.-G. Vesicular and Tubular Structures Prepared from Self-Assembly of Novel Amphiphilic ABA Triblock Copolymers in Aqueous Solutions. *J. Polym. Sci., Part A: Polym. Chem.* **2008**, *46*, 1042−1050.

(14) Guo, C.; Luo, Y.; Zhou, R.; Wei, G. Probing the Self-Assembly Mechanism of Diphenylalanine-Based Peptide Nanovesicles and Nanotubes. *ACS Nano* **2012**, *6*, 3907−3918.

(15) Valery, C.; Artzner, F.; Paternostre, M. Peptide Nanotubes: Molecular Organisations, Self-Assembly Mechanisms and Applications. *Soft Matter* **2011**, *7*, 9583−9594.

(16) Krieg, E.; Shirman, E.; Weissman, H.; Shimoni, E.; Wolf, S. G.; Pinkas, I.; Rybtchinski, B. Supramolecular Gel Based on a Perylene Diimide Dye: Multiple Stimuli Responsiveness, Robustness, and Photofunction. *J. Am. Chem. Soc.* **2009**, *131*, 14365−14373.

(17) Ustinov, A.; Weissman, H.; Shirman, E.; Pinkas, I.; Zuo, X.; Rybtchinski, B. Supramolecular Polymers in Aqueous Medium: Rational Design Based on Directional Hydrophobic Interactions. *J. Am. Chem. Soc.* **2011**, *133*, 16201−16211.

(18) Percec, V.; Wilson, D. A.; Leowanawat, P.; Wilson, C. J.; Hughes, A. D.; Kaucher, M. S.; Hammer, D. A.; Levine, D. H.; Kim, A. J.; Bates, F. S.; Davis, K. P.; Lodge, T. P.; Klein, M. L.; DeVane, R. H.; Aqad, E.; Rosen, B. M.; Argintaru, A. O.; Sienkowska, M. J.; Rissanen, K.; Nummelin, S.; Ropponen, J. Self-Assembly of Janus Dendrimers into Uniform Dendrimersomes and Other Complex Architectures. *Science* **2010**, *328*, 1009−1014.

(19) Shahar, C.; Dutta, S.; Weissman, H.; Shimon, L. J. W.; Ott, H.; Rybtchinski, B. Precrystalline Aggregates Enable Control over Organic Crystallization in Solution. *Angew. Chem.* **2016**, *128*, 187−190.

(20) Cui, H.; Hodgdon, T. K.; Kaler, E. W.; Abezgauz, L.; Danino, D.; Lubovsky, M.; Talmon, Y.; Pochan, D. J. Elucidating the Assembled Structure of Amphiphiles in Solution *via* Cryogenic Transmission Electron Microscopy. *Soft Matter* **2007**, *3*, 945−955.

(21) Ziserman, L.; Lee, H.-Y.; Raghavan, S. R.; Mor, A.; Danino, D. Unraveling the Mechanism of Nanotube Formation by Chiral Self-Assembly of Amphiphiles. *J. Am. Chem. Soc.* **2011**, *133*, 2511−2517.

(22) Golubkov, G.; Weissman, H.; Shirman, E.; Wolf, S. G.; Pinkas, I.; Rybtchinski, B. Economical Design in Noncovalent Nanoscale Synthesis: Diverse Photofunctional Nanostructures Based on a Single Covalent Building Block. *Angew. Chem., Int. Ed.* **2009**, *48*, 926−930.

(23) Weissman, H.; Rybtchinski, B. Noncovalent Self-Assembly in Aqueous Medium: Mechanistic Insights from Time-Resolved Cryogenic Electron Microscopy. *Curr. Opin. Colloid Interface Sci.* **2012**, *17*, 330−342.

(24) Baram, J.; Weissman, H.; Tidhar, Y.; Pinkas, I.; Rybtchinski, B. Hydrophobic Self-Assembly Affords Robust Noncovalent Polymer Isomers. *Angew. Chem., Int. Ed.* **2014**, *53*, 4123−4126.

(25) Glotzer, S. C.; Solomon, M. J. Anisotropy of Building Blocks and Their Assembly into Complex Structures. *Nat. Mater.* **2007**, *6*, 557−562.

(26) Barry, E.; Dogic, Z. Entropy Driven Self-Assembly of Nonamphiphilic Colloidal Membranes. *Proc. Natl. Acad. Sci. U. S. A.* **2010**, *107*, 10348−10353.

(27) Angert, I.; Burmester, C.; Dinges, C.; Rose, H.; Schröder, R. R. Elastic and Inelastic Scattering Cross-Sections of Amorphous Layers of Carbon and Vitrified Ice. *Ultramicroscopy* **1996**, *63*, 181−192.

(28) Tidhar, Y.; Weissman, H.; Wolf, S. G.; Gulino, A.; Rybtchinski, B. Pathway-Dependent Self-Assembly of Perylene Diimide/Peptide Conjugates in Aqueous Medium. *Chem. - Eur. J.* **2011**, *17*, 6068−6075.

(29) Gillissen, M. A. J.; Koenigs, M. M. E.; Spiering, J. J. H.; Vekemans, J. A. J. M.; Palmans, A. R. A.; Voets, I. K.; Meijer, E. W. Triple Helix Formation in Amphiphilic Discotics: Demystifying Solvent Effects in Supramolecular Self-Assembly. *J. Am. Chem. Soc.* **2014**, *136*, 336−343.

(30) Balbo Block, M. A.; Kaiser, C.; Khan, A.; Hecht, S., Discrete Organic Nanotubes Based on a Combination of Covalent and Non-Covalent Approaches. In *Functional Molecular Nanostructures*; Schlüter, A. D., Ed.; Springer: Berlin, Heidelberg, 2005; pp 89−150.

(31) Besenius, P. Controlling Supramolecular Polymerization Through Multicomponent Self-Assembly. *J. Polym. Sci., Part A: Polym. Chem.* **2017**, *55*, 34−78.

(32) Würthner, F.; Saha-Möller, C. R.; Fimmel, B.; Ogi, S.; Leowanawat, P.; Schmidt, D. Perylene Bisimide Dye Assemblies as Archetype Functional Supramolecular Materials. *Chem. Rev.* **2016**, *116*, 962−1052.

(33) Gosztola, D.; Niemczyk, M. P.; Svec, W.; Lukas, A. S.; Wasielewski, M. R. Excited Doublet States of Electrochemically Generated Aromatic Imide and Diimide Radical Anions. *J. Phys. Chem. A* **2000**, *104*, 6545−6551.

(34) Shirman, E.; Ustinov, A.; Ben-Shitrit, N.; Weissman, H.; Iron, M. A.; Cohen, R.; Rybtchinski, B. Stable Aromatic Dianion in Water. *J. Phys. Chem. B* **2008**, *112*, 8855−8858.

(35) Norris, J. R.; Uphaus, R. A.; Crespi, H. L.; Katz, J. J. Electron Spin Resonance of Chlorophyll and the Origin of Signal I in Photosynthesis. *Proc. Natl. Acad. Sci. U. S. A.* **1971**, *68*, 625−628.

(36) Wilson, T. M.; Zeidan, T. A.; Hariharan, M.; Lewis, F. D.; Wasielewski, M. R. Electron Hopping among Cofacially Stacked Perylenediimides Assembled by using DNA Hairpins. *Angew. Chem., Int. Ed.* **2010**, *49*, 2385−2388.

(37) Wu, Y.; Young, R. M.; Frasconi, M.; Schneebeli, S. T.; Spenst, P.; Gardner, D. M.; Brown, K. E.; Würthner, F.; Stoddart, J. F.; Wasielewski, M. R. Ultrafast Photoinduced Symmetry-Breaking

DOI: 10.1021/acsnano.7b06376
ACS Nano 2018, 12, 317−326

Charge Separation and Electron Sharing in Perylenediimide Molecular Triangles. *J. Am. Chem. Soc.* **2015**, *137*, 13236−13239.
(38) Spenst, P.; Young, R. M.; Wasielewski, M. R.; Wurthner, F. Guest and Solvent Modulated Photo-Driven Charge Separation and Triplet Generation in a Perylene Bisimide Cyclophane. *Chem. Sci.* **2016**, *7*, 5428−5434.
(39) Marciniak, H.; Li, X.-Q.; Würthner, F.; Lochbrunner, S. One-Dimensional Exciton Diffusion in Perylene Bisimide Aggregates. *J. Phys. Chem. A* **2011**, *115*, 648−654.
(40) Vauthey, E. Photoinduced Symmetry-Breaking Charge Separation. *ChemPhysChem* **2012**, *13*, 2001−2011.
(41) Vuković, L.; Madriaga, A.; Kuzmis, A.; Banerjee, A.; Tang, A.; Tao, K.; Shah, N.; Král, P.; Onyuksel, H. Solubilization of Therapeutic Agents in Micellar Nanomedicines. *Langmuir* **2013**, *29*, 15747−15754.
(42) Vuković, L.; Khatib, F. A.; Drake, S. P.; Madriaga, A.; Brandenburg, K. S.; Král, P.; Onyuksel, H. Structure and Dynamics of Highly PEG-ylated Sterically Stabilized Micelles in Aqueous Media. *J. Am. Chem. Soc.* **2011**, *133*, 13481−13488.
(43) Brunsveld, L.; Folmer, B. J. B.; Meijer, E. W.; Sijbesma, R. P. Supramolecular Polymers. *Chem. Rev.* **2001**, *101*, 4071.
(44) Sosso, G. C.; Chen, J.; Cox, S. J.; Fitzner, M.; Pedevilla, P.; Zen, A.; Michaelides, A. Crystal Nucleation in Liquids: Open Questions and Future Challenges in Molecular Dynamics Simulations. *Chem. Rev.* **2016**, *116*, 7078−7116.
(45) Cohen, E.; Weissman, H.; Shimoni, E.; Kaplan-Ashiri, I.; Werle, K.; Wohlleben, W.; Rybtchinski, B. Robust Aqua Material: A Pressure-Resistant Self-Assembled Membrane for Water Purification. *Angew. Chem., Int. Ed.* **2017**, *56*, 2203−2207.
(46) Wilson, T. M.; Tauber, M. J.; Wasielewski, M. R. Toward an n-Type Molecular Wire: Electron Hopping within Linearly Linked Perylenediimide Oligomers. *J. Am. Chem. Soc.* **2009**, *131*, 8952−8957.
(47) MacKerell, A. D., Jr; Bashford, D.; Bellott, M.; Dunbrack, R. L., Jr; Evanseck, J. D.; Field, M. J.; Fischer, S.; Gao, J.; Guo, H.; Ha, S.; et al. All-Atom Empirical Potential for Molecular Modeling and Dynamics Studies of Proteins. *J. Phys. Chem. B* **1998**, *102*, 3586−3616.
(48) Vanommeslaeghe, K.; Hatcher, E.; Acharya, C.; Kundu, S.; Zhong, S.; Shim, J.; Darian, E.; Guvench, O.; Lopes, P.; Vorobyov, I.; MacKerell, A. D. CHARMM General Force Field (CGenFF): A Force Field for Drug-like Molecules Compatible with the CHARMM All-Atom Additive Biological Force Fields. *J. Comput. Chem.* **2010**, *31*, 671−690.
(49) Vanommeslaeghe, K.; MacKerell, A. D. Automation of the CHARMM General Force Field (CGenFF) I: Bond Perception and Atom Typing. *J. Chem. Inf. Model.* **2012**, *52*, 3144−3154.
(50) Vanommeslaeghe, K.; Raman, E. P.; MacKerell, A. D. Automation of the CHARMM General Force Field (CGenFF) II: Assignment of Bonded Parameters and Partial Atomic Charges. *J. Chem. Inf. Model.* **2012**, *52*, 3155−3168.
(51) Yu, W.; He, X.; Vanommeslaeghe, K.; MacKerell, A. D. Extension of the CHARMM General Force Field to Sulfonyl-Containing Compounds and its Utility in Biomolecular Simulations. *J. Comput. Chem.* **2012**, *33*, 2451−2468.
(52) *CHARMM General Force Field (CGenFF)*, https://cgenff.paramchem.org/ (accessed November 4, 2016).
(53) Frisch, M. J.; Trucks, G. W.; Schlegel, H. B.; Scuseria, G. E.; Robb, M. A.; Cheeseman, J. R.; Scalmani, G.; Barone, V.; Petersson, G. A.; Nakatsuji, H.; Li, X.; Caricato, M.; Marenich, A. V.; Bloino, J.; Janesko, B. G.; Gomperts, R.; Mennucci, B.; Hratchian, H. P.; Ortiz, J. V.; Izmaylov, A. F.; Sonnenberg, J. L.; Williams-Young, D.; Ding, F.; Lipparini, F.; Egidi, F.; Goings, J.; Peng, B.; Petrone, A.; Henderson, T.; Ranasinghe, D.; Zakrzewski, V. G.; Gao, J.; Rega, N.; Zheng, G.; Liang, W.; Hada, M.; Ehara, M.; Toyota, K.; Fukuda, R.; Hasegawa, J.; Ishida, M.; Nakajima, T.; Honda, Y.; Kitao, O.; Nakai, H.; Vreven, T.; Throssell, K.; Montgomery, J. A., Jr.; Peralta, J. E.; Ogliaro, F.; Bearpark, M. J.; Heyd, J. J.; Brothers, E. N.; Kudin, K. N.; Staroverov, V. N.; Keith, T. A.; Kobayashi, R.; Normand, J.; Raghavachari, K.; Rendell, A. P.; Burant, J. C.; Iyengar, S. S.; Tomasi, J.; Cossi, M.; Millam, J. M.; Klene, M.; Adamo, C.; Cammi, R.; Ochterski, J. W.; Martin, R. L.; Morokuma, K.; Farkas, O.; Foresman, J. B.; Fox, D. J. *Gaussian 09*; Gaussian, Inc.: Wallingford, CT, 2013.
(54) Breneman, C. M.; Wiberg, K. B. Determining Atom-Centered Monopoles from Molecular Electrostatic Potentials. The Need for High Sampling Density in Formamide Conformational Analysis. *J. Comput. Chem.* **1990**, *11*, 361−373.
(55) Belandria, V.; Mohammadi, A. H.; Richon, D. Volumetric Properties of the (Tetrahydrofuran + Water) and (Tetra-n-butyl ammonium bromide + Water) Systems: Experimental Measurements and Correlations. *J. Chem. Thermodyn.* **2009**, *41*, 1382−1386.
(56) Darden, T.; York, D.; Pedersen, L. Particle Mesh Ewald: An N·log(N) Method for Ewald Sums in Large Systems. *J. Chem. Phys.* **1993**, *98*, 10089−10092.

DOI: 10.1021/acsnano.7b06376
ACS Nano 2018, 12, 317−326